Nanoscale Advances

ROYAL SOCIETY OF CHEMISTRY

PAPER

View Article Online
View Journal | View Issue

Cite this: *Nanoscale Adv.*, 2025, **7**, 5361

Cobalt–nickel metal–organic frameworks (CNMs) as drug delivery agents for triple-negative breast cancer†

Shaik Sameer Basha, Abhishek Sasmal, Subastri Ariraman, Mukilarasi B, Thilak Raj, Vimalraj Selvaraj, A. Arockiarajan and Swathi Sudhakar *

Breast cancer is one of the most prevalent cancers worldwide, with triple-negative breast cancer (TNBC) representing a particularly aggressive subtype, making it difficult to treat, and is associated with a poor prognosis. However, chemotherapy is associated with challenges such as drug resistance, off-target toxicity, and limited efficacy, highlighting the need for more effective therapies. Nanocarriers, including liposomes, micelles, and dendrimers, offer improved drug delivery efficacy and reduced toxicity but face challenges in terms of stability and scalability. Metal–organic frameworks (MOFs) have emerged as promising drug delivery systems, particularly for combination therapies to overcome resistance in TNBC. In this study, cobalt–nickel metal–organic frameworks (CNMs) were synthesized and loaded with a combination of cisplatin (Cis), doxorubicin (Dox), and 5-fluorouracil (5-Fu) (MD-CNM) to develop a novel multidrug delivery system. The MD-CNM exhibited high biocompatibility, an efficient drug loading capacity of 95.44 ± 4.05%, and sustained release over 96 h. Moreover, the MD-CNM demonstrated potent cytotoxicity against MDA-MB-231 breast cancer cells, with an IC_{50} concentration of 461 nM, which is two- to five-fold less than the IC_{50} value of individual drugs (Cis, Dox, and 5-Fu) loaded with the CNM, indicating enhanced therapeutic efficacy. Additionally, flow cytometry analysis revealed that the MD-CNM induced necrosis (77.59%) and late apoptosis (12.37%) with cell cycle arrest in the G_0/G_1 phase, further confirming its anticancer potential. Furthermore, the *ex ovo* chorioallantoic membrane (CAM) assay demonstrated that the MD-CNM significantly inhibited tumor angiogenesis by downregulating key pro-angiogenic factors, including vascular endothelial growth factor A (VEGFA), fibroblast growth factor 2 (FGF2), and angiopoietin 1 (ANG1) within the tumor microenvironment. These findings underscore the potential of CNMs as an innovative and efficient multidrug delivery platform for targeted cancer therapy, particularly for treating TNBC, offering a promising alternative to conventional chemotherapy with improved efficacy and reduced toxicity.

Received 26th February 2025
Accepted 2nd July 2025

DOI: 10.1039/d5na00193e

rsc.li/nanoscale-advances

1 Introduction

Triple-negative breast cancer (TNBC) accounts for approximately 10–20% of all breast cancer cases, with higher prevalence in younger women and those of African descent.[1,2] TNBC is recognized as particularly aggressive and difficult to treat.[3] TNBC is defined by the absence of estrogen receptors (ER), progesterone receptors (PR), and human epidermal growth factor receptor 2 (HER2).[4] This lack of targeted receptors limits treatment options, making TNBC notably challenging to manage compared to other breast cancer subtypes. The aggressive nature of TNBC is characterized by rapid tumor growth and a higher likelihood of metastasis, often spreading to visceral organs such as the lungs and brain, complicating treatment strategies.[5] Furthermore, patients diagnosed with TNBC are at an increased risk of recurrence, especially in the first few years after treatment. Additionally, the poor prognosis associated with breast cancer, particularly TNBC, is often linked to late-stage diagnosis and the absence of precise biomarkers. However, recent advances in diagnostic technologies, such as surface-enhanced Raman spectroscopy (SERS) and inflammation index-based screening, offer potential for earlier detection and risk stratification, enabling timely and personalized therapeutic interventions.[6,7]

Chemotherapy is the cornerstone of TNBC treatment, with common regimens including anthracyclines and taxanes.[8,9] While chemotherapy can be effective in controlling tumors, it is associated with significant limitations. Many patients resist these chemotherapeutic agents over time, leading to reduced efficacy.[10,11] Furthermore, chemotherapy's nontarget action affects both cancerous and healthy cells, resulting in off-target

Department of Applied Mechanics and Biomedical Engineering, Indian Institute of Technology Madras, Chennai-600036, India. E-mail: swathi.s@iitm.ac.in

† Electronic supplementary information (ESI) available. See DOI: https://doi.org/10.1039/d5na00193e

toxicity and side effects such as nausea, fatigue, and increased risk of infections. The overall survival (OS) for advanced TNBC with chemotherapy is often limited, highlighting the need for more effective and targeted treatment strategies that can minimize systemic toxicity and improve clinical outcomes.[12,13]

Nanocarriers have garnered significant attention for their potential to address the challenges of conventional chemotherapy in TNBC treatment. These nanoscale delivery systems can enhance drug solubility, improve the targeting of tumor sites, and minimize systemic toxicity.[14] These types of nanocarriers include liposomes,[15,16] micelles,[17,18] dendrimers,[19] metals[20] and polymeric nanoparticles.[21]

Despite their promise, the clinical translation of nanocarriers faces several challenges. Issues such as poor stability in biological environments, limited drug-loading capacity, and potential immunogenic responses can reduce their effectiveness.[22,23] For instance, some nanocarriers may degrade prematurely in the bloodstream, releasing the drug.[24,25] Research has shown that poly(lactic-*co*-glycolic acid) (PLGA) nanoparticles can undergo degradation when exposed to physiological conditions, which can lead to the release of their drug payload before reaching the targeted tissue.[26] Alternatively, recent advances in nanomedicine have explored stimuli-responsive systems, such as redox-sensitive disulfide-linked assemblies, which enable tumor-specific drug release *via* elevated intracellular glutathione levels.[27] However, manufacturing nanocarriers with consistent quality and scaling up production for clinical use remain significant hurdles.[28]

To overcome the limitations of conventional chemotherapy and nanocarriers, metal–organic frameworks (MOFs) have emerged as innovative drug delivery platforms.[29] MOFs are crystalline materials composed of metal ions and organic linkers, offering a high surface area, tunable porosity, and structural flexibility.[30,31] These properties make MOFs suitable for encapsulating a wide range of therapeutic agents, including small molecules, proteins, and nucleic acids. MOFs are particularly advantageous for combinational drug therapy, an approach that uses multiple drugs to target different pathways in cancer cells, thereby improving the therapeutic efficacy and reducing the likelihood of drug resistance.[32,33] The large surface area and tunable pore size of MOFs allow for the co-loading of multiple drugs with controlled release profiles. For instance, MOFs can release one drug in response to a specific stimulus, such as pH changes in the tumor microenvironment, while simultaneously releasing another drug under different conditions.[34,35] This capability makes MOFs highly versatile for developing multidrug delivery systems tailored to the complex biology of TNBC.

Despite their advantages, MOFs face limitations that must be addressed for clinical application. Stability under physiological conditions is still a major concern. For instance, some MOFs may degrade or release toxic components when exposed to biological fluids.[36] Additionally, the synthesis of MOFs is often resource-intensive and may involve toxic solvents, raising concerns about scalability and safety. Further research is needed to optimize MOF stability, reduce cytotoxicity, and streamline manufacturing processes. Previous reports suggest that, as compared to single elemental nanomaterials, the alloy-based ones possess improved physicochemical properties like enhanced stability and mitigated toxicity.[37] Yet, this has not been utilized effectively in developing alloy-based MOF nanocarriers specifically in drug delivery applications. Also, MOFs' application in the cancer therapeutic field is still in its nascent stages.

Hence, in this work, we present a novel bimetallic cobalt–nickel-based metal–organic framework (CNM) as a nanoscale multidrug delivery platform for TNBC therapy which has not been reported for the same purpose elsewhere. The CNM was transformed into a multidrug nanocarrier platform (MD-CNM) by co-encapsulating three chemotherapeutic drugs cisplatin (Cis), doxorubicin (Dox), and 5-fluorouracil (5-Fu). The MD-CNM was found to possess exceptionally high drug loading efficiency and demonstrated sustained drug release. Furthermore, *in vitro* studies were conducted to confirm the biocompatible nature of CNM with NIH-3T3 cell lines and the potent cytotoxicity of MD-CNM against MDA-MB-231 TNBC cells. Furthermore, the MD-CNM's anti-angiogenic potential was validated using the *ex ovo* chorioallantoic membrane (CAM) assay. Overall, this work shows the potential of an MOF-based drug delivery platform in TNBC therapeutics, offering an alternative to conventional monotherapy and non-specific drug delivery strategies.

2 Materials and methodology

2.1. Synthesis of cobalt–nickel metal–organic frameworks (CNMs)

The cobalt–nickel metal–organic frameworks (CNMs) were fabricated *via* a modified hydrothermal method, as mentioned by Abhishek Sasmal *et al.*[38] First, 2.88 mM (0.4784 g) terephthalic acid (benzene-1,4-dicarboxylic acid, BDC, 98% grade, SRL Chemicals) was taken in a 70 mL dimethylformamide (DMF, Merck, Mumbai, India), 5 mL distilled deionized water (Evergreen, Chennai, India), and 5 mL absolute ethanol (Merck) solvent mixture. Dissolution was carried out at room temperature while stirring the mixture with a magnetic stirrer. After the complete dissolution of BDC, 1.44 mM nickel nitrate hexahydrate ($Ni(NO_3)_2 \cdot 6H_2O$, 98% SRL Chemicals) was added along with cobalt nitrate hexahydrate ($Co(NO_3)_2 \cdot 6H_2O$, 98% SRL Chemicals) in turn under stirring and dissolved. The resulting mixture was infiltrated with ultrasound for approximately 30 minutes and magnetically stirred for about 10–15 minutes. The mixed solution was then transferred into a 100 mL Teflon-lined stainless-steel autoclave, and the entire solution was kept in an oven maintained at 125 °C for 15 hours. Then, the autoclave was depressurized after allowing it to reach room temperature. A centrifuge was employed to obtain the precipitate, which was washed with distilled ethanol three times. Finally, the obtained precipitate was placed in a 50 degrees Celsius oven for around 5 hours and lightly ground to get the Co–Ni MOF powder.

2.2. Characterization of the CNM

2.2.1. Scanning electron microscopy (SEM). The morphological characterization of the CNM was carried out using

a scanning electron microscope (Apreo S-SEM, EDS; Thermo Scientific). A very dilute (1 : 100) dispersion of the MOF in water was prepared and drop-cast (10 μL) onto a pre-cleaned glass slide. The solvent was allowed to evaporate at room temperature. Afterward, the MOF sample was sputter-coated with a thin layer of gold–palladium alloy using a Polaron SC7640 gold sputter coater, operating at 5 kV and 20 mA with a deposition rate of 10 nm per minute. Scanning electron microscopy (SEM) analysis was performed at an operating voltage of 1–5 kV to examine the morphology of the MOF. The elemental composition of the CNM was further confirmed using energy dispersive X-ray spectroscopy (EDX).

2.3. Drug loading efficiency of the CNM

Before drug loading, a multidrug solution was prepared by mixing cisplatin (Cis), 5-fluorouracil (5-Fu), and doxorubicin (Dox) in a 1 : 1 : 1 molar ratio. To synthesize the multidrug-loaded CNM (MD-CNM), equal volumes of CNM solution (1 mg mL^{-1}) and the multidrug solution were mixed to yield the final multidrug concentration as 50 μM, which correspond to 16.67 μM of each drug and stirred at 300 rpm on a magnetic stirrer (BR Biochem) for 12 hours. After incubation, the samples were centrifuged at 13 000 rpm for 30 minutes, and the supernatant was collected to quantify drug loading using high-performance liquid chromatography (HPLC) (Shimadzu LC-2050C) to assess the free drug concentration.

For HPLC analysis, the sample was injected into a C18 analytical column at a flow rate of 1 mL min^{-1} and maintained at 37 °C. The mobile phase for cisplatin consisted of methanol (HPLC grade) and 0.9% sodium chloride (NaCl) in a 10 : 90 (v/v) ratio.[39] For doxorubicin, the mobile phase comprised acetonitrile (HPLC grade) and formic acid in a 99 : 1 (v/v) ratio.[40] For 5-fluorouracil, methanol and water in a 10 : 90 (v/v) ratio with the pH adjusted to 3.2 were used as the mobile phase.[41] The HPLC data were processed using LC Solution software to quantify the free drug concentration, and the drug loading efficiency (DLE%) was calculated using the following formula.

$$\text{DLE } \% = \frac{\text{total drug concentration} - \text{free drug concentration}}{\text{total drug concentration}} \times 100$$

Post-drug loading, the MD-CNM was characterized using SEM and EDX analyses similar to the CNM.

2.4. Fourier transform infrared (FTIR) spectroscopy

To further investigate the multi drug interactions with the CNM, Fourier transform infrared (FTIR) analysis was conducted using an FTIR spectrophotometer (TENSOR II, Bruker Optics) in the transmission wavelength range of 600–4000 cm^{-1}. For this analysis, the samples were prepared by pelletizing the MOF with potassium bromide (KBr) in a 1 : 100 (% w/w) ratio using a hydraulic pressure mold, applying pressure in the range of 0.5–1.5 Pa.

2.5. *In vitro* multidrug release kinetics of CNM

The drug release kinetics of the MD-CNM were experimentally evaluated using the dialysis membrane method.[42,43] In this setup, a dialysis membrane pouch containing the MD-CNM was submerged in a glass beaker filled with 1× phosphate-buffered saline (PBS) at physiological pH (7.4), and also with acidic pH 6, with continuous stirring at 150 rpm. At specific time intervals (0.5, 1, 2, 3, 4, 8, 12, 24, 36, 48, 60, 72, 84, and 96 h), fixed volumes of the sample were withdrawn to measure the amount of drug released. The drug concentration in the samples was quantified using high-performance liquid chromatography (HPLC) (Shimadzu LC-2050C). The drug release percentage of the samples of individual time was calculated using the following formula:

$$\text{Drug release}\% = \frac{\text{amount of released drug}}{\text{total drug amount}} \times 100$$

2.6. *In vitro* cell culture studies

2.6.1. Cell lines and cell culture. The embryonic mouse fibroblast cell line (NIH 3T3) and the multidrug-resistant breast cancer cell line (MDA-MB-231) were obtained from the National Centre for Cell Science (NCCS), Pune. Agar culture confirmed that both cell lines were free from mycoplasma contamination. The cells were cultured in Dulbecco's Modified Eagle's Medium (DMEM), supplemented with 10% fetal bovine serum (FBS) and 1% penicillin–streptomycin antibiotic solution (containing 10 000 units of penicillin and 10 mg of streptomycin in 0.9% NaCl) (Himedia) and maintained in a 5% CO_2 atmosphere at 37 °C.

2.6.2. Biocompatibility of CNM cell viability assessment using MTT. The biocompatibility of the CNM was evaluated using the NIH 3T3 embryonic mouse fibroblast cell line employing the MTT (3-[4,5-dimethylthiazol-2-yl]-2,5 diphenyl tetrazolium bromide) assay, which measures the cell viability based on the activity of mitochondrial dehydrogenase enzymes.[44,45] Briefly, the NIH 3T3 cells were seeded into 96-well tissue culture plates at a density of 5×10^3 cells per well and allowed to adhere for 24 hours under a 5% CO_2 atmosphere at 37 °C using a Thermo Scientific Forma Steri-Cycle incubator. Subsequently, NIH 3T3 cells were treated with varying concentrations of CNM (0.1, 0.5, 1, 1.5, and 2 μg mL^{-1}) to assess biocompatibility. After the treatment period of 24 hours, the culture media was removed, and 100 μL of MTT solution (0.5 μg mL^{-1}) was added to each well. The plates were then incubated for an additional 4 hours in the dark to allow for the reduction of MTT by mitochondrial dehydrogenase enzymes, resulting in the formation of formazan crystals. Following incubation, the MTT solution was discarded, and 100 μL of dimethyl sulfoxide (DMSO) was added to dissolve the formazan crystals. The absorbance was subsequently measured at 570 nm using a multimode microplate reader (BioTek H1M Synergy). The percentage of cell viability was calculated using the following formula:

$$\text{Cell viability}\% = \left(\frac{\text{absorbance of treated cells}}{\text{absorbance of control cells}}\right) \times 100$$

2.6.3. Cytotoxicity of the multidrug-loaded CNM (MD-CNM). Additionally, the cytotoxicity of the MD-CNM was assessed on the MDA-MB-231 multidrug-resistant breast cancer cell lines using the MTT assay. Briefly, MDA-MB-231 cells were seeded into 96-well tissue culture plates at a density of 5×10^3 cells per well and allowed to adhere for 24 hours. Following adhesion, for cytotoxicity evaluations, MDA-MB-231 cells were exposed to different concentrations of CNM (1, 1.5, 2, 3, 4, 4.5, and 5 μg mL^{-1}), as well as the MD-CNM, multidrug alone, and individual drugs (cisplatin (Cis), 5-fluorouracil (5-Fu), and doxorubicin (Dox)) at concentrations of 100, 200, 400, 600, 800, 1000, 2000, 5000, and 10 000 nM for 24 hours. The MTT assay was then performed as described in the previous section to evaluate cell viability.

2.7. Morphological studies of cells using acridine orange (AO)/ethidium bromide (EBr) staining

The effect of MD-CNM on triple-negative breast cancer cell (MDA-MB-231) toxicity was investigated morphologically using fluorescence microscopy, with cells labeled using acridine orange (AO) and ethidium bromide (EBr).[15] Using this method, viable cells are differentiated from the cells undergoing cell death (apoptosis or necrosis). Briefly, MDA-MB-231 cells were seeded at a density of 1×10^5 cells per mL in a cell culture plate and treated with MD-CNM at its IC_{50} concentration. After 24 hours of incubation, the culture media was removed, and the cells were washed with 1× phosphate-buffered saline (PBS) (pH 7.4). A fluorescent dye solution containing equal amounts of AO and EBr (100 μg mL^{-1}) was added to the cells, followed by a 30 minute incubation. The cells were then washed again with 1× PBS and observed under a fluorescence microscope (inverted Nikon Eclipse Ti–U) for morphological examination of cell toxicity.

2.8. Phalloidin/Hoechst staining for cytoskeletal analysis

To investigate the effect of MD-CNM on F-actin cytoskeletal derangement, MDA-MB-231 cells were seeded in a 6-well culture plate at a density of 2×10^5 cells per mL and incubated for 24 hours at 37 °C in a 5% CO_2 atmosphere. After the incubation period, the cells were treated with MD-CNM at IC_{50} concentration and incubated further. Following treatment, the cells were fixed with 4% paraformaldehyde (PFA) and 0.5% Triton-X for 15 minutes. After fixation, the cells were washed with 1× PBS. The cells were then stained with 50 μL of phalloidin (1×, Invitrogen) to visualize F-actin filaments and incubated for 1 hour. Next, 10 μL of Hoechst (10 μg mL^{-1}, Thermo Fisher) was used to counterstain the nuclei, followed by a 30 minute incubation and a final wash with 1× PBS. Imaging was performed using a Nikon Eclipse Ti–U fluorescence microscope. The merged images of phalloidin-stained F-actin filaments and Hoechst-stained nuclei were analyzed using ImageJ software to assess cytoskeletal changes.

2.9. Fluorescence-activated cell sorting (FACS) analysis

The mechanism of cell death (apoptosis or necrosis) induced by MD-CNM in MDA-MB-231 cells was elucidated using flow cytometry (FACS analysis) following the manufacturer's instructions. Cell death was quantified using allophycocyanin (APC)-labeled Annexin V, a calcium-binding protein that fluorescently detects phosphatidylserine on the membrane of apoptotic cells. To distinguish between apoptotic and necrotic cells, propidium iodide (PI) was used as a co-stain.[45] For this analysis, MDA-MB-231 cells were seeded at a density of 1×10^5 cells per plate and incubated for 24 hours. The cells were then treated with MD-CNM at IC_{50} concentration for 24 hours. After treatment, both non-adherent and adherent cells were collected, centrifuged at 1500 rpm for 5 minutes, and washed twice with cold 1× PBS. The cell pellet was resuspended in 1× binding buffer (10 mM HEPES, 140 mM sodium chloride, and 2.5 mM calcium chloride) to enhance efficient dye binding. Next, 2 μL of Annexin V-APC (4 μg mL^{-1}) and 2 μL of propidium iodide (PI, 1 mg mL^{-1}) were added to the cell suspension, which was gently vortexed and incubated in the dark. Unstained and single-stained controls (for Annexin V and PI) were used for fluorochrome compensation. Apoptosis and necrosis were then quantified using flow cytometry (BD FACS CANTO II), and the data were analyzed with CytExpert software version 2.4.

2.10. Cell cycle analysis

The cell cycle phases of MDA_MB-231 breast cancer cells were analyzed using a Beckman Coulter flow cytometer equipped with CytExpert software (version 2.4). Cells were treated with MD-CNM at IC_{50} concentration and incubated for 24 h. After incubation, the cells were harvested *via* centrifugation and washed with ice-cold 1× PBS. Fixation was performed using 70% cold ethanol at −20 °C for a minimum of 2 h. The fixed cells were subsequently rinsed with 1× PBS by centrifugation at 1500 rpm for 5 minutes. For staining, the cells were incubated at 4 °C for 15 minutes in a solution containing propidium iodide (12 μg mL^{-1}) and ribonuclease A (10 μg mL^{-1}) in 0.1% Triton-X buffer. Flow cytometry analysis was conducted, and the results were processed using CytExpert software (version 2.4).

2.11. Effect of MD-CNM on tumor-induced angiogenesis through the CAM assay model

Next, the chick embryo chorioallantoic membrane (CAM) assay was employed to evaluate the angiogenetic properties of the MD-CNM. The CAM, an extraembryonic membrane in chick embryos that is highly vascularized and immunodeficient, makes it an ideal model for mimicking the tumor microenvironment (TEM). This model's exceptional properties allow us to facilitate the study of tumor angiogenesis, including forming new blood vessels and interacting with the tumor and its surroundings.[46] Tumors often establish a TEM characterized by hypoxia, acidosis, and high interstitial pressure, which stimulate the release of pro-angiogenic factors, promoting blood vessel formation to sustain tumor growth.[46] The CAM assay replicates these conditions, allowing for studying tumor-induced angiogenesis. For this study, fertilized eggs were incubated in a ventilated, humidified egg incubator at 37 °C. On day 3, embryos were transferred into sterile containers (*ex ovo*) and incubated for another 2–3 days. On day 5, the embryos were

classified into four groups: (group-1) a control group, with no sample or tumor added to the CMA bed; (group-2) tumor group, wherein to induce tumor formation, 5×10^3 MDA-MB-231 cells were pre-cultured on 18 mm coverslips and carefully placed on the CAM surface of fertilized eggs on day 5 of incubation in an *ex ovo* setup based on the protocols established elsewhere.[47,48] This setup allowed direct interaction between tumor cells and the CAM, which facilitates localized tumor formation and mimics tumor-induced angiogenesis. (group-3) MDA-MB-231 cells with bare CNM placed on the CAM bed; (group-4) as a positive control for angiogenesis inhibition, a group of embryos received Avastin (bevacizumab), a VEGF-targeting monoclonal antibody, topically applied along with tumor cells at a concentration of 10 mM as reported previously,[49] and finally MDA-MB-231 cells were treated with MD-CNM at IC_{50} concentration and placed on the CAM bed. Angiogenesis was assessed by imaging the CAM vasculature at 0, 5, and 10 h post-treatment using a stereomicroscope (Olympus, India) equipped with a Magnus digital camera. The acquired images were analyzed with IKOSA CAM software (**https://www.kmlvision.com/our-offerings/ikosa-prisma/**), which quantified angiogenic parameters, namely the vessel area, vessel length, mean vessel thickness, and branching nodes. Comparison of these parameters across the groups helps reveal the effects of CNM and MD-CNM on tumor angiogenesis and determine their impact on vascular network formation and functionality.

2.11.1. Anti-angiogenetic effect of MD-CNM using gene expression study through RT-PCR. Additionally, to confirm the anti-angiogenic effect of MD-CNM at the molecular level, Reverse Transcription Polymerase Chain Reaction (RT-PCR) was performed to evaluate the expression levels of angiogenic genes, Vascular Endothelial Growth Factor A (VEGFA), Fibroblast Growth Factor 2 (FGF2), and Angiopoietin 1 (ANG1). After CAM exposure to MD-CNM (for 10 h), total RNA was isolated from the CAM tissues using TRIzol reagent (Invitrogen, USA), following the manufacturer's instructions. The RNA concentration and purity were measured with a NanoDrop 2000 spectrophotometer (Thermo Scientific, USA), ensuring an absorbance ratio of 260 : 280 nm within the range of 1.8–2.0. From 1 μg of total RNA, complementary DNA (cDNA) was synthesized using a Reverse Transcriptase Kit (Invitrogen, USA), adhering to the protocol provided by the manufacturer. Gene expression levels were analyzed using a KAPA SYBR FAST qPCR Kit (Kapa Biosystems, MA, USA) with primers specific to VEGFA, FGF2, ANG1, and the housekeeping gene β-actin (refer to Table 1 for primer sequences). The qPCRs were carried out in a total reaction volume of 20 μL under conditions of initial denaturation at 95 °C for 3 minutes, followed by amplification cycles (40 cycles) with denaturation at 95 °C for 10 seconds and annealing/extension at 60 °C for 30 seconds, during which fluorescence data were collected. Then, the C_t values were normalized to the housekeeping gene (β-actin), and the fold change in gene expression was calculated using the delta–delta C_t ($\Delta\Delta C_t$) method.[50] This analysis provides insights into the regulation of angiogenic markers, allowing for a detailed understanding of the molecular impact of MD-CNM on tumor-induced angiogenesis.

Table 1 The list of primers used for the study

Primers	Sequence (5′ to 3′ and 3′ to 5′)	
Chicken FGF-2	Forward	AGAGGAGTAGTATCAATCAAAG
	Reverse	TGCCACATACCAATCAGAGT
Chicken ANG-1	Forward	GAGTCTGGTCACTCGGCAAA
	Reverse	CTAGGCTGCCATCTTCTCGG
Chicken VEGFA	Forward	TGAGGGCCTAGAATGTGTCC
	Reverse	TCTTTTGACCCTTCCCCTTT
Chicken β-actin	Forward	TCTGACTGACCGCGTTACTC
	Reverse	CCATCACACCCTGATGTCTG

3 Results and discussion

3.1. Characterization of the CNM and MD-CNM

The morphology of the CNM and MD-CNM was analyzed by scanning electron microscopy (SEM), as shown in Fig. 1. The pristine CNM (Fig. 1a) exhibits a smooth, crystalline surface with well-defined polyhedral structures, indicative of its highly ordered and rigid framework. The absence of visible deformation in the pristine CNM confirms the stability and robustness of its architecture. In contrast, post-drug loading, the surface of MD-CNM shows slight distortion of polyhedral edges, likely due to the deposition of drug molecules on the MOF surface and within the pores (Fig. 1b). This could be attributed to the interaction between the MOF and multidrug molecules. Furthermore, the elemental analysis using EDX showed the presence of Co and Ni in CNM and the elements corresponding to the respective drugs over the surface of the MD-CNM (refer Fig. SI-1†).

3.2. Multidrug encapsulation efficiency and release kinetics of multidrug-loaded CNM (MD-CNM)

To evaluate the drug loading of the cobalt–nickel metal–organic framework (CNM) and release kinetics of multidrug-loaded CNM (MD-CNM), the HPLC technique was employed. The CNM was incubated with a combinational drug solution (50 μM) for 12 h at room temperature, and multidrug loading was determined. Table 2 presents the load concentration of each drug in the MD-CNM formulation and also the corresponding drug loading efficiency. We then quantified the multidrug loading efficacy of the MD-CNM as 97.5 ± 3.4% (48.75 μM). The high efficiency underscores the potential of CNM as a versatile drug carrier system. The observed high loading efficiency can be

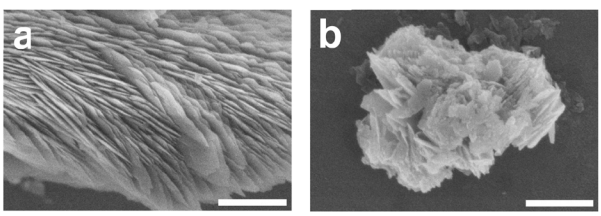

Fig. 1 SEM images showing the surface morphologies of (a) CNM and (b) MD-CNM. Scale bar: 1 μm.

Table 2 Loading efficiency of each drug in MD-CNM

Drug	Individual concentration of the loaded drug (μM)	Individual loading percentage of drug (%)
Cisplatin	16.33	98 ± 3.3
Doxorubicin	16.25	97.5 ± 2.8
5-Fluorouracil	16.17	97 ± 4
Total	48.75	97.5 ± 3.4

attributed to the unique structural and chemical properties of CNM, including its large surface area,[51,52] and the presence of functional groups[53] that enable effective drug absorption and binding. These properties enable the encapsulation of diverse drugs with different physiochemical characteristics, expanding the scope of the CNM for multidrug delivery applications and highlights the potential of the CNM as a robust multidrug carrier system for cancer therapy.

Next, the release kinetics of MD-CNM were analyzed under two physiologically relevant pH conditions of pH 7.4, representative of normal physiological environments, and pH 6.0, simulating the acidic tumour or endosomal microenvironment. The drug release experiment was conducted over 96 hours (Fig. 2). A distinct pH-dependent release behaviour was observed, characterized by a markedly faster release at acidic pH, which is highly desirable for targeted cancer drug delivery. At 0.5 hours, cumulative drug release was 1.61 ± 0.03% at pH 7.4 and 2.13 ± 0.09% at pH 6.0, which increased to 4.03 ± 0.06% and 6.74 ± 0.14% at 1 hour, and further to 5.99 ± 0.20% and 10.83 ± 0.61% at 2 hours, respectively. A burst-type release under acidic conditions became evident by 3 hours, with 7.99 ± 0.53% at pH 7.4 and 17.66 ± 0.92% at pH 6.0. At 4 hours, the values reached 12.66 ± 1.31% and 23.50 ± 1.31% at pH 7.4 and 6.0, respectively. This continued to diverge at 8 hours, where cumulative release reached 21.66 ± 1.59% (pH 7.4) and 53.67 ± 1.57% (pH 6.0). After 12 hours, release was 35.99 ± 1.50% at pH 7.4 and 70.68 ± 1.77% at pH 6.0. By 24 hours, release at pH 6.0 achieved a near-complete release of 91.01 ± 1.80%, while only 49.33 ± 1.62% was observed at pH 7.4. A full 100% release at pH 6.0 was achieved by 36 hours and maintained thereafter. In contrast, pH 7.4 showed a more gradual increase: 57.66 ± 1.54% at 36 hours, 76.91 ± 1.77% at 48 hours, 91.63 ± 1.70% at 60 hours, 96.65 ± 2.06% at 72 hours, and 100% by 96 hours.

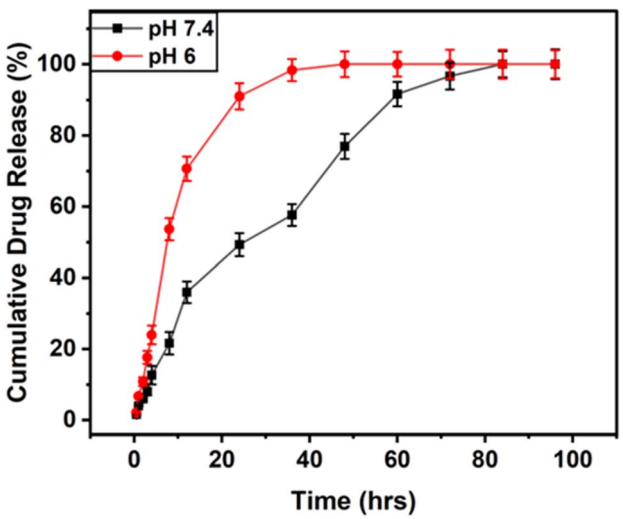

Fig. 2 Cumulative multidrug release profiles of MD-CNM at pH 7.4 (physiological) and pH 6.0 (acidic) across increasing time intervals.

This drug release profile confirms the pH-responsiveness of the MD-CNM system, with an accelerated release under acidic conditions and a sustained and controlled release under physiological pH. The acidic environment likely triggers protonation and partial framework degradation, promoting drug diffusion.[45,48] This ensures the effective accumulation of drugs at the tumor site while minimizing systemic exposure. Furthermore, the total multidrug release was normalized to 48.75 μM, and the molarity-based cumulative release profile is provided in Fig. SI-2a,† with individual drug release profiles (cisplatin, 5-fluorouracil, and doxorubicin) plotted separately in Fig. SI-2b and c† corresponding to pH 7.4 and 6, respectively, confirming consistent proportional release relative to the initial loading. The multidrug release profiles in terms of molarity at pH 7.4 and pH 6 provide better clarity of the release profiles of individual drugs.

Comparison of the release profiles between the drugs showed that a significant difference was observed, with cisplatin exhibiting a slower release rate than doxorubicin and 5-fluorouracil. This slower release can be attributed to stronger interactions between cisplatin and the CNM, likely through metal–ligand coordination.[54] This biphasic release pattern observed in MD-CNM aligns with previously reported MOF-based drug delivery systems,[55] where the initial burst release ensures an immediate drug payload, followed by a sustained release phase that maintains therapeutic drug levels over an extended period. This controlled release mechanism reduces the dosing frequency and minimizes potential side effects, enhancing the treatment efficacy.[56]

3.3. Fourier transform infrared spectral analysis of MD-CNM

Next, to confirm the successful incorporation of 5-fluorouracil, cisplatin, and doxorubicin into the CNM, forming the multidrug-loaded CNM (MD-CNM) (Fig. 3), FTIR analysis was performed. For 5-fluorouracil, the distinctive C=O stretching at 1666 cm^{-1} and peaks at 833 cm^{-1} and 625 cm^{-1} for out-of-plane bending vibrations were preserved, confirming its presence.[57,58] Similarly, cisplatin exhibited its characteristic N–H bending at 1626 cm^{-1} and Pt–Cl stretching at 802 cm^{-1}, which were also detected in MD-CNM with slight shifts, indicating successful interaction with the MOF.[42,43] Doxorubicin's signature O–H stretching at 3284 cm^{-1} and C=O stretching at 2730 cm^{-1} were similarly observed, confirming its interaction with the MOF.[15] Shifts in peaks such as the O–H stretching at 3599 cm^{-1}, along with new bands at 2924 cm^{-1} and 2851 cm^{-1} for C–H stretching, indicate the formation of hydrogen bonds and interactions between the drugs and the MOF matrix.

The structural integrity of the CNM was maintained after drug loading, as evidenced by the retention of key peaks like the

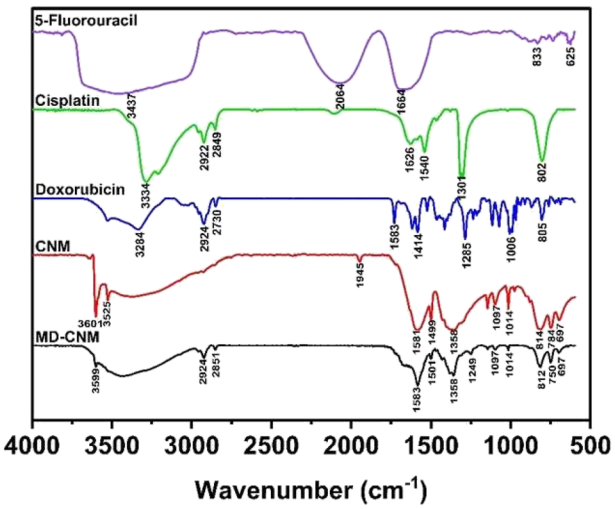

Fig. 3 FTIR spectral analysis of CNM, MD-CNM, and individual drugs (cisplatin, doxorubicin, and 5-fluorouracil), illustrating characteristic functional group vibrations and confirming successful drug incorporation into the MOF.

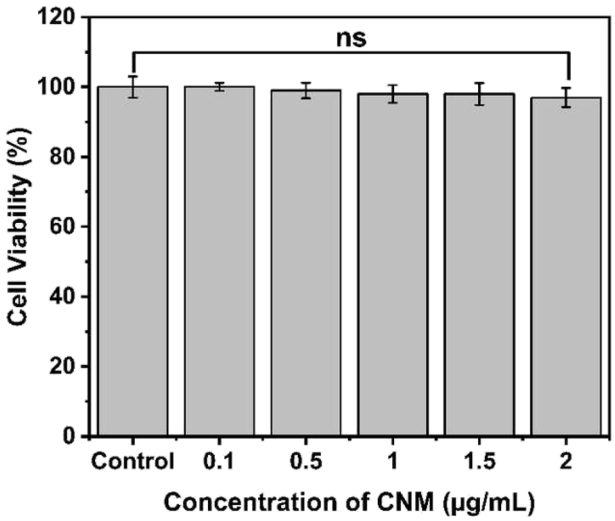

Fig. 4 MTT assay result depicting the cell viability (%) of control (untreated) and CNM (0.1–2 μg mL^{-1})-treated NIH-3T3 cells after 24 hours of incubation. Statistical analysis was done by the *T* test. The symbol "ns" denotes no statistical difference between the cell viability values at different concentrations.

carboxylate asymmetric and symmetric stretching at 1583 cm^{-1} and 1414 cm^{-1}, characteristic of the MOF structure. Additional peaks in the fingerprint region (1000–700 cm^{-1}) further confirm that the CNM remained intact. The spectral changes, such as broadening and intensity variations, highlight interactions such as hydrogen bonding and coordination between the drugs and the MOF metal centres. The stability of the framework and the shifts in drug-specific peaks are consistent with reports of MOFs, forming stable host–guest complexes through hydrogen bonding, π–π interactions, and metal–ligand coordination.[59,60] Overall, the FTIR analysis confirms the successful preparation of the MD-CNM with all three drugs loaded synergistically while preserving the structural stability of the MOF.

3.4. Biocompatibility of the CNM in NIH 3T3 cells

The application of cobalt–nickel metal–organic frameworks (CNMs) in anticancer therapy necessitates a comprehensive understanding of their safety and biological effects. Therefore, we evaluated the biocompatibility of CNMs using the MTT assay on NIH 3T3 fibroblast cell lines. Fig. 4 presents the biocompatibility of the CNM evaluated using NIH 3T3 fibroblast cells at concentrations (0.1, 0.5, 1, 1.5, and 2 μg mL^{-1}), and the results demonstrated excellent cell viability.

At the lowest concentration of 0.1 μg mL^{-1}, the cell viability was 100 ± 1.16%, indicating no cytotoxic effects. Even as the concentration increased, the cell viability remained constant, with 99 ± 2.17%, 98 ± 2.5%, 98 ± 3.1%, and 97 ± 2.7% observed at 0.5, 1, 1.5, and 2 μg mL^{-1}, respectively. These findings confirm that the CNM exhibits remarkable biocompatibility even at higher concentrations.

3.5. *In vitro* cytotoxic effect of MD-CNM in triple-negative breast cancer cells MDA-MB-231

3.5.1. *In vitro* cytotoxicity analysis. Next, the *in vitro* anticancer efficacy of multidrug-loaded CNM (MD-CNM) was evaluated against MDA-MB-231 breast cancer cells at various concentrations (100, 200, 400, 600, 800, 1000, 2000, 5000, and 10 000 nM), and the results were compared with CNM alone, multidrug alone, and CNM loaded with individual drugs (cisplatin, doxorubicin, and 5-fluorouracil) at the same concentrations. The cell viability significantly decreased ($p < 0.05$) with increasing concentrations of MD-CNM. At concentrations of 100, 200, 400, 600, 800, 1000, 2000, 5000, and 10 000 nM, the observed cell viabilities were 99 ± 3.48%, 80 ± 2.8%, 60 ± 3.08%, 42 ± 3.6%, 21 ± 4.38%, 2 ± 2.8%, 1 ± 0.58%, 0 ± 0.08%, and 0 ± 0.08%, respectively (Fig. 5a). In comparison, individual drug-loaded CNMs exhibited reduced cytotoxicity at equivalent concentrations (Fig. 5b). Cisplatin-loaded CNMs showed cell viabilities of 100 ± 3.2%, 100 ± 2.6%, 90 ± 2.8%, 80 ± 3.4%, 70 ± 4.1%, 60 ± 2.4%, 40 ± 1.3%, 25 ± 1.8%, and 13 ± 0.6%, respectively. Similarly, for 5-fluorouracil-loaded CNMs, the corresponding viabilities were 99 ± 2.6%, 95 ± 1.5%, 90 ± 2.8%, 80 ± 2.3%, 82 ± 1.6%, 71 ± 1.7%, 59 ± 1.3%, 30 ± 0.6%, and 14 ± 0.63%. Doxorubicin-loaded CNMs demonstrated viabilities of 98 ± 1.8%, 90 ± 2.6%, 80 ± 2.4%, 70 ± 1.7%, 62 ± 1.6%, 51 ± 2.3%, 30 ± 1.2%, 15 ± 2.1%, and 3 ± 1%.

From the cell viability assay, we quantified the IC_{50} concentration of multidrug loaded MD-CNM to be 461 nM, which gives the final concentration of each drug as 154.4 nM, 153.8 nM, and 153.0 nM for cisplatin, doxorubicin, and 5-fluorouracil, respectively, and the corresponding CNM concentration is 4.61 μg mL^{-1}. Additionally, we observed that CNM alone exhibited minimal inherent cytotoxicity towards MDA-MB-231 breast cancer cells (Fig. SI-3a†) with cell viability >75% at the highest tested concentration of 5 μg mL^{-1}. Studies reveal that MOFs based on cobalt have anticancer properties at higher concentrations. For example, cobalt MOFs have been demonstrated to trigger apoptosis in cancer cells, decreasing the cell viability and

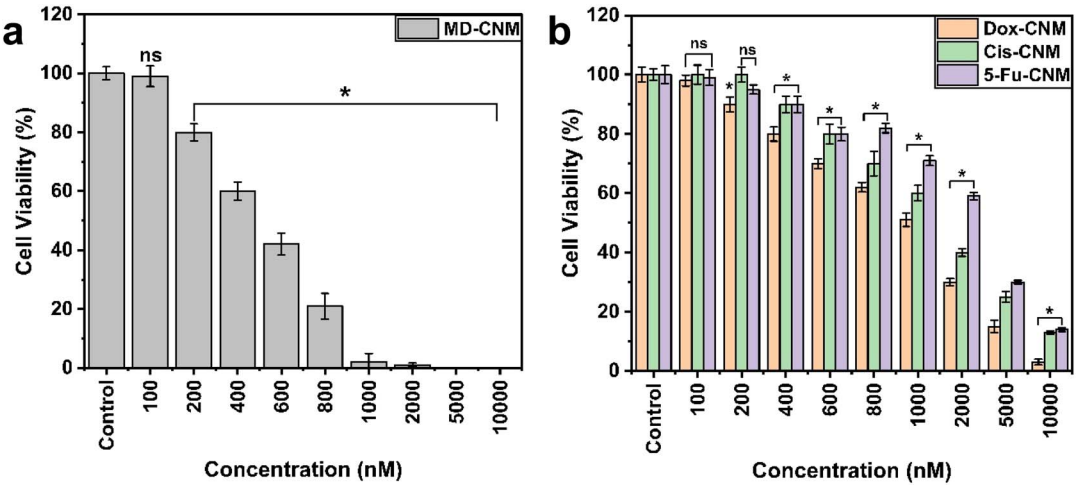

Fig. 5 MTT assay result depicting the cell viability (%) of MDA-MB-231 cells treated with (a) control and the multidrug-loaded CNM (MD-CNM) (100–10000 nM) and (b) control and the CNM loaded with doxorubicin (Dox-CNM), cisplatin (Cis-CNM), and 5-fluorouracil (5-Fu-CNM) (100–10000 nM). Statistical analysis was done by the *T* test. The symbol "*" denotes statistical difference between the cell viability values at different concentrations with $p < 0.05$, and the symbol "ns" denotes no statistical difference between the cell viability values at different concentrations with $p > 0.05$.

tumor development by inducing reactive oxygen species (ROS).[61,62] The distinct characteristics of the nickel and cobalt ions in MOFs may potentially improve the efficacy of combination treatments.[61,63] Through enhanced medication transport and increased local concentrations of therapeutic drugs at tumor locations, these metal ions can reduce systemic toxicity and enhance anticancer effects in combination.[64] However, the MD-CNMs were found to be cytotoxic against cancer cell lines at very low concentrations, and comparison of the same with bare CNM at similar concentrations confirms that the cell death induced by the MD-CNM is due to the drugs loaded into the CNM nanoplatform. Furthermore, the multidrug alone treatment also showed cytotoxicity, with an IC_{50} concentration of 743 nM (Fig. SI-3b†), which is 1.6-fold higher than that of MD-CNM, further demonstrating the superior effectiveness of MD-CNM. Also, the MD-CNM's IC_{50} value is significantly lower than the IC_{50} values of the free drug-loaded CNMs, which were 1.5 μM, 2.84 μM, and 1.1 μM for cisplatin, 5-fluorouracil, and doxorubicin, respectively. As for the free drugs (cisplatin, doxorubicin, and 5-fluorouracil), their cytotoxic effects on MDA-MB-231 triple-negative breast cancer cells have been extensively studied and reported in the literature. For instance, a previous study reported the IC_{50} concentration of 40 μM for cisplatin against MDA-MB-231 TNBC cell lines.[65] Furthermore, doxorubicin and 5-fluorouracil were found to exhibit IC_{50} concentrations of 6.5 μM and 29 μM, respectively, in the same cell line.[66,67] In comparison, the MD-CNM's extremely low IC_{50} value validates its enhanced therapeutic potential as compared with the free drugs' values from the literature. This superior efficacy of MD-CNM can be attributed to its ability to deliver a synergistic combination of anticancer drugs in a controlled manner, enhancing the therapeutic effect. The results emphasize the potential of MD-CNM as a highly effective platform for combination therapy, reducing drug dosages while maintaining robust anticancer activity. This finding supports the growing interest in MOF-based drug delivery systems, promising strategies for overcoming the limitations of conventional single-drug treatments.

3.5.2. Cell death effect of MD-CNM on MDA-MB-231 cells by AO/EBr dual staining. To further evaluate what MD-CNM on MDA-MB-231 cells exhibit cell death (apoptosis or necrosis), we performed an acridine orange/ethidium bromide (AO/EB) dual staining assay (Fig. 6). This assay allows differentiation between viable, apoptotic, and necrotic cells based on the integrity of the cellular and nuclear structures. In untreated control cells, normal cellular morphology was observed, characterized by intact nuclei emitting green fluorescence, indicative of healthy, viable cells. In contrast, MD-CNM-treated cancer cells exhibited significant morphological changes associated with apoptosis, such as extensive nuclear condensation and late apoptotic-related cell death. These changes were evident from the orange and red fluorescence emitted by the stained cells after 24 hours of treatment, highlighting the induction of both apoptotic and necrotic pathways.

The observed nuclear damage in MD-CNM-treated cells may be attributed to oxidative stress induced by the framework. Cobalt and nickel ions within the MD-CNM are known to generate reactive oxygen species (ROS), which can disrupt mitochondrial function and damage nuclear DNA, triggering apoptotic pathways.[68] The dual staining results underscore the effectiveness of MD-CNM in inducing programmed cell death through apoptosis alongside necrosis, offering a dual-mode cytotoxicity mechanism that enhances the therapeutic efficacy. Importantly, MD-CNM demonstrated a high degree of specificity in targeting MDA-MB-231 cells, a triple-negative breast cancer (TNBC) model, without exhibiting cytotoxicity toward normal cells as it minimizes off-target effects and preserves the viability of healthy tissues. The combinatorial drug delivery

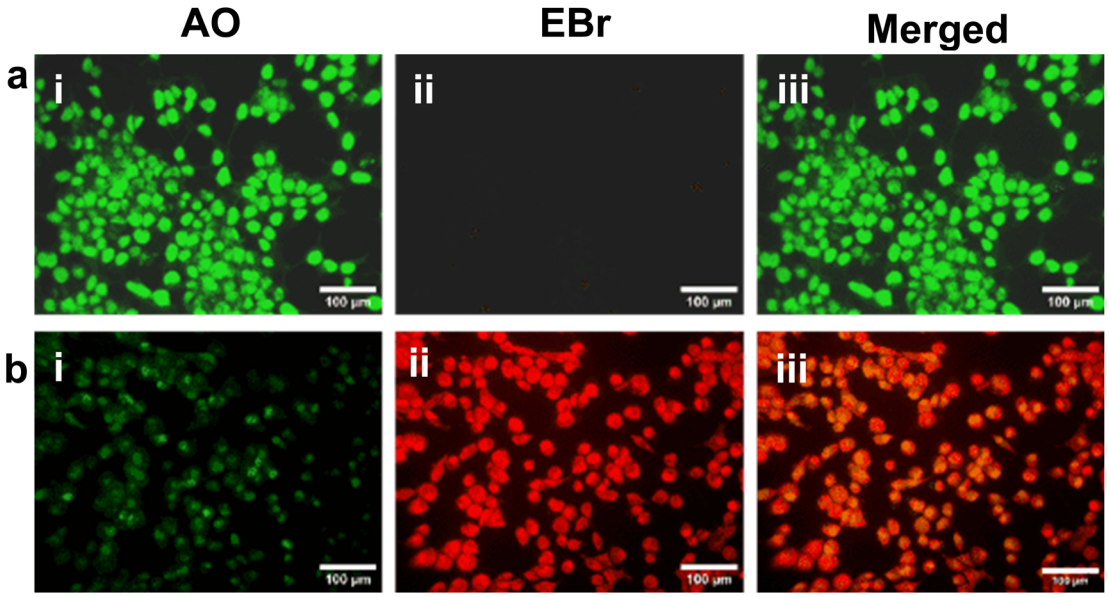

Fig. 6 Fluorescence images of (a) untreated cells and (b) MD-CNM (461 nM)-treated MDA-MB-231 cells using the AO/EBr staining method (Live/Dead assay), with each column corresponding to (i) AO stained, (ii) EBr stained, and (iii) merged images of cells stained with AO/EBr.

capability of MD-CNM enables synergistic effects, allowing multiple drugs to act on different pathways[69] within cancer cells.

3.5.3. Effect of MD-CNM on cytoskeleton organization of MDA-MB-231 cells. To further investigate the impact of MD-CNM on cytoskeletal organization, a phalloidin–Hoechst staining assay was conducted on MDA-MB-231 cell lines, and the results are presented in Fig. 7. In untreated cells, normal cytoskeletal architecture was evident, characterized by organized actin filaments and intact nuclear structures (Fig. 7a). However, MD-CNM treatment at IC_{50} concentration induced significant alterations in the cytoskeletal arrangement. The treated cells displayed disrupted actin filament organization and nuclear disarray compared to the untreated control group (Fig. 7b). MD-CNM treatment significantly disrupts the cytoskeletal organization in MDA-MB-231 cells, a process likely driven by the generation of reactive oxygen species (ROS). Cytoskeletal components in healthy cells are highly organized, playing essential roles in maintaining the cell shape and their transport, and division. However, elevated ROS levels, induced by chemotherapeutic agents like cisplatin (Cis), 5-fluorouracil (5-Fu), and doxorubicin (Dox), can destabilize actin filaments

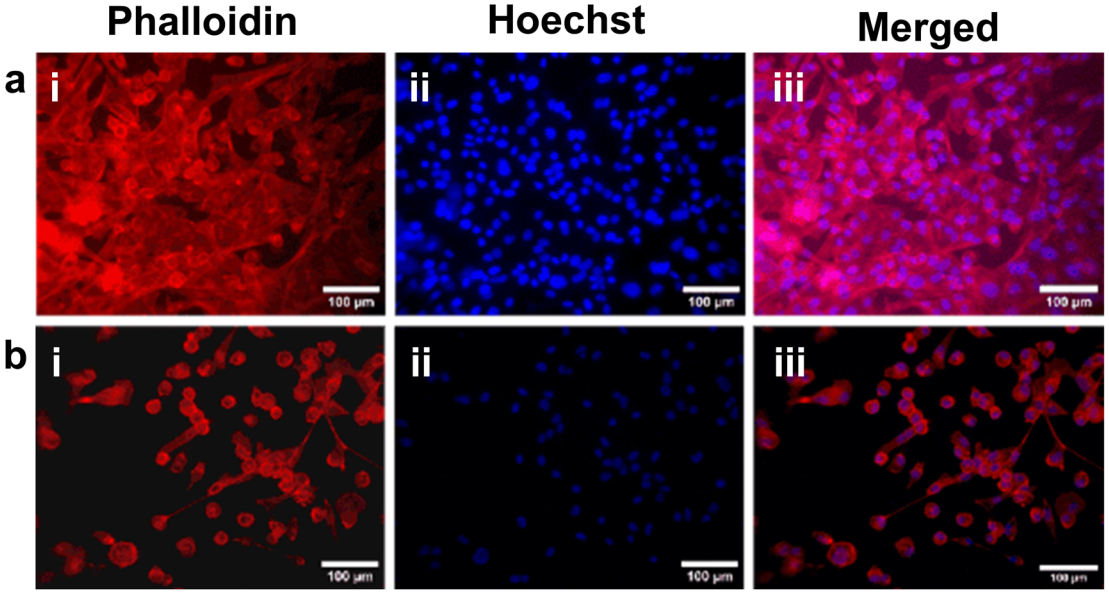

Fig. 7 Phalloidin–Hoechst staining of MDA-MB-231 cell lines that are (a) untreated (control) and (b) treated with MD-CNM (461 nM), with each column corresponding to (i) phalloidin stained, (ii) Hoechst stained, and (iii) merged images of cells stained with phalloidin and Hoechst.

and associated proteins.[15,70,71] This disruption leads to structural abnormalities and ultimately results in cellular apoptosis or necrosis.

The study demonstrates that the MD-CNM effectively alters the actin cytoskeleton, impairing critical cellular functions such as adhesion, motility, and division.[72] This disruption of cytoskeletal dynamics highlights the role of ROS-mediated oxidative stress in the cytotoxicity of the MD-CNM.[73] The findings emphasize its dual therapeutic potential: inducing cell death and limiting metastasis in aggressive cancers like triple-negative breast cancer (TNBC).[74]

3.5.4. FACS analysis of MD-CNM-treated MDA-MB-231 cells. To gain a deeper understanding of the cellular mechanisms underlying the cytotoxicity of MD-CNM, flow cytometry-based detection of apoptosis and necrosis was performed using Annexin V-APC/PI staining. Annexin V, a calcium-binding protein, was fluorescently labeled to detect phosphatidylserine externalization on the membranes of apoptotic cells. Propidium iodide (PI) co-staining was employed to differentiate necrotic cells from apoptotic ones, providing a comprehensive assessment of cell death modes, including necroapoptosis, a regulated form of cell death exhibiting features of both apoptosis and necrosis.

The analysis began by identifying a homogeneous population of MDA-MB-231 cells using forward and side scatter plots (Fig. 8a). Following treatment with MD-CNM, a significant induction of necrosis was observed, with 77.59% of cells undergoing necrosis (Fig. 8c). In contrast, the control group exhibited 95.73% cell viability (Fig. 8b). Late apoptosis was observed in 12.37% of treated cells, while early apoptosis was minimal, accounting for only 0.05%. The results also indicated potential necroapoptosis in the MD-CNM-treated cells, as the overlap between apoptotic and necrotic markers suggested a regulated pathway contributing to the cell death profile. Necroapoptosis, which bridges the mechanisms of necrosis and apoptosis, can provide therapeutic advantages by enabling controlled cell death without triggering excessive inflammation.

These findings underscore the robust cytotoxic effect of MD-CNM on MDA-MB-231 cells, with a significant predominance of necrosis over apoptosis. The increase in necrotic cells, the minimal early apoptosis, and the possibility of necro apoptosis suggest that the MD-CNM exerts a multifaceted mechanism of cell death. Importantly, the predominance of necroapoptosis may reduce inflammatory responses often associated with uncontrolled cell death,[75] making MD-CNM a promising candidate for therapeutic applications. This characteristic is particularly advantageous in cancer treatment, where achieving controlled and effective cytotoxicity is critical for improving treatment outcomes. The MD-CNM may cause necroptosis mechanistically by phosphorylating Mixed Lineage Kinase Domain-Like protein (MLKL), disrupting membranes, and activating Receptor-Interaction Protein Kinase (RIPK) RIPK1/RIPK3 signaling.[76] Oxidative stress and activation of the necroptotic pathway might result from the metal ions in the CNM increasing ROS. Furthermore, the MD-CNM may suppress caspase activation, causing necroptosis rather than apoptosis in cell death. DAMPs may be released by mitochondrial failure brought on by the MD-CNM, which would further trigger necroptosis.[77,78] This mechanism provides regulated cell death and possible immunogenic effects in cancer therapy, increasing the therapeutic effectiveness of MD-CNM, especially in apoptosis-resistant MDA-MB-231 cells.

3.5.5. Effect of MD-CNM on cell cycle arrest. Next, flow cytometry cell cycle analysis was conducted to evaluate cells' distribution across different cell cycle phases. As shown in Fig. 9a, the control cells exhibited the following phase distribution: shows that around Sub-G1 (5.57%), G0/G1 (69.18%), S (18.65%), and G2/M (6.6%). In the MD-CNM-treated cells (Fig. 9b), 11.9%, 82.64%, 3.66%, and 1.8% cells were observed at the Sub-G1, G0/G1, S, and G2/M phases. The findings indicate that the MD-CNM induced significant cell cycle arrest at the Sub-G1, and G0/G1 phases compared to the control. Specifically, MD-CNM treatment resulted in 2.13-fold and 1.19-fold increased cell arrest in the Sub-G1 and G0/G1 phases related to control cells (Fig. 9c). Moreover, a pronounced reduction in the

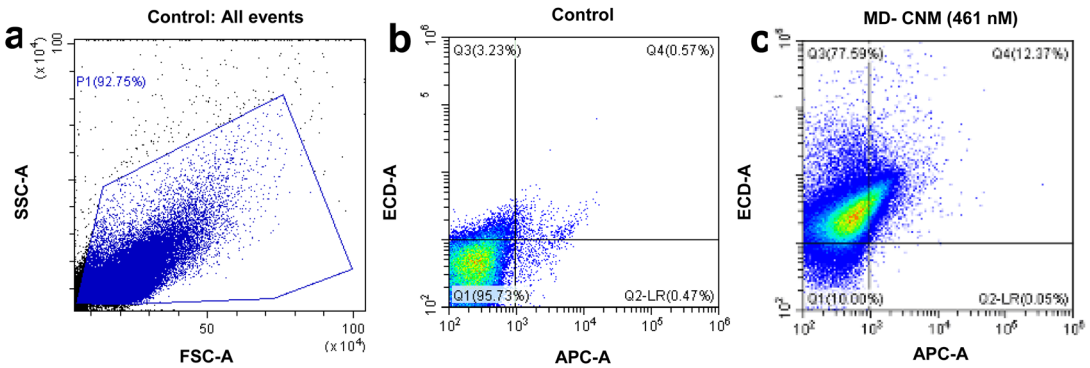

Fig. 8 FACS evaluation of MDA-MB-231-labeled cells for quantification of apoptosis/necrosis induced by MD-CNM: (a) MDA-MB-231 cells gated on forward and side scatter dot plots; (b) and (c) dot plots of untreated and treated cells with MD-CNM, respectively. The lower left quadrant (Q1) shows the percentage of total living cells (Annexin V and PI negative). The lower right quadrant (Q2) indicates early apoptotic cells (Annexin V positive/PI negative), the upper left quadrant (Q3) represents necrotic cells (Annexin V negative/PI positive), and the upper right quadrant (Q4) represents late apoptotic cells (both Annexin V and PI positive).

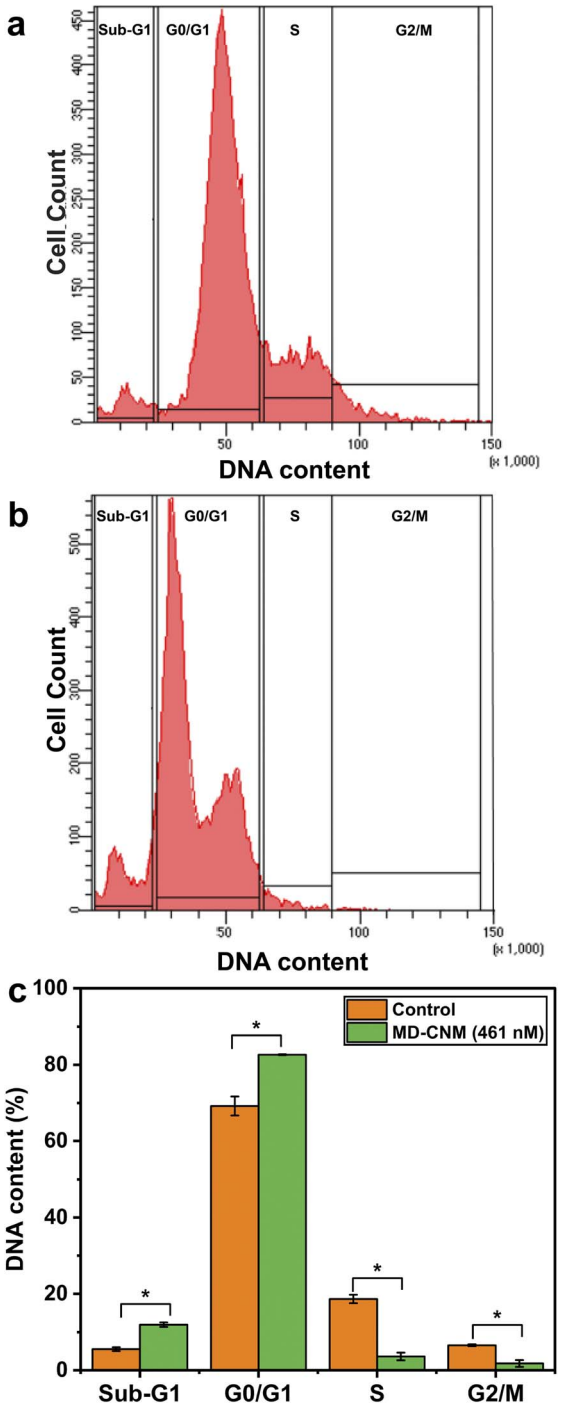

Fig. 9 Cell cycle profiles of (a) untreated (control) and (b) MD-CNM (461 nM)-treated breast cancer cells (MDA-MB-231) through flow cytometry with propidium iodide staining. (c) Bar graph showing the percentage of cell cycle distribution between control and treated cells. The symbol "*" represents the significance level at $p < 0.05$ as compared to control.

proportion of cells in the S and G1/M phases was observed with 5-fold and 3.6-fold decreases, respectively, in the MD-CNM-treated cells compared to controls.

These results are consistent with the idea that MD-CNM induces apoptosis or programmed cell death. The increased Sub-G1 population reflects apoptosis, which may be driven by DNA damage, mitochondrial dysfunction, or endoplasmic reticulum stress. DNA damage activates checkpoint proteins that can trigger apoptotic pathways if the damage is irreparable. Additionally, mitochondrial dysfunction, a common target of anticancer drugs, may release pro-apoptotic factors, and ER stress can also promote apoptotic signals.[79] The G0/G1 phase arrest further implies that MD-CNM inhibits progression into the S phase. This may occur through the inhibition of cyclin-dependent kinases (CDKs), which are critical for the G1/S transition, or through the upregulation of CDK inhibitors that suppress the CDK activity.[80] Additionally, interference with key growth signaling pathways that regulate cell cycle progression could play a role in this arrest.[81] Finally, while the MD-CNM does not seem to induce a direct G2/M arrest, its effect on early-phase progression could indirectly affect G2/M by disrupting mitotic processes and causing a backlog in earlier stages of the cycle.[73] Together, these findings underscore the potent anti-cancer efficacy of MD-CNM, particularly against triple-negative breast cancer (TNBC). By effectively inducing cell cycle arrest at the early interphase stages, MD-CNM limits the proliferative capacity of cancer cells, providing a strong foundation for its potential therapeutic applications.

3.6. Angiogenic effect of MD-CNM using the CAM assay

Angiogenesis is crucial in tumor progression and metastasis. This study evaluated the anti-angiogenic potential of MD-CNM using the CAM assay. Images of the CAM model were captured, processed through ImageJ software and analyzed with a tool named IKOSA (Fig. 10a). The key angiogenic parameters, including vessel area, total vessel length, vessel thickness, and vessel nodes were measured at 0, 5, and 10 h (Fig. 10b), where vessel area indicates the overall extent of the vascular network, vessel length reflects the vascular complexity and density, mean vessel thickness represents the structural integrity of blood vessels, and branching nodes measure the network's capacity for blood distribution.

The tumor group showed a significant increase in all angiogenic parameters compared to the control, emphasizing the tumor microenvironment's (TEM) pro-angiogenic effects. At 5 and 10 h, the vessel area (2.18- and 2.4-fold), vessel length (2.14- and 1.8-fold), thickness (1.6- and 2-fold), and nodes (1.8- and 1.4-fold) were increased markedly, indicative of abnormal and excessive angiogenesis, a hallmark of tumor progression. Vascular disorganization is a characteristic of pathological angiogenesis, with an irregular vessel structure and branching patterns.[82] CNM treatment alone resulted in a slight reduction in angiogenic parameters compared to the tumor group, suggesting that the CNM carrier itself has some anti-angiogenic effects that can counteract the angiogenic stimulus induced by the tumor microenvironment. Additionally, the CNM demonstrated cytotoxicity against MDA-MB-231. Consequently, embryos treated with MD-CNM exhibited a profound reduction in the vessel area (2.47- and 2.5-fold), vessel length (2.02- and 2-fold), thickness (1.5- and 2.06-fold), and nodes (1.73- and 1.82-fold) in all angiogenic parameters at 5 and 10 hours compared to the tumor group, demonstrating the potent anti-angiogenic

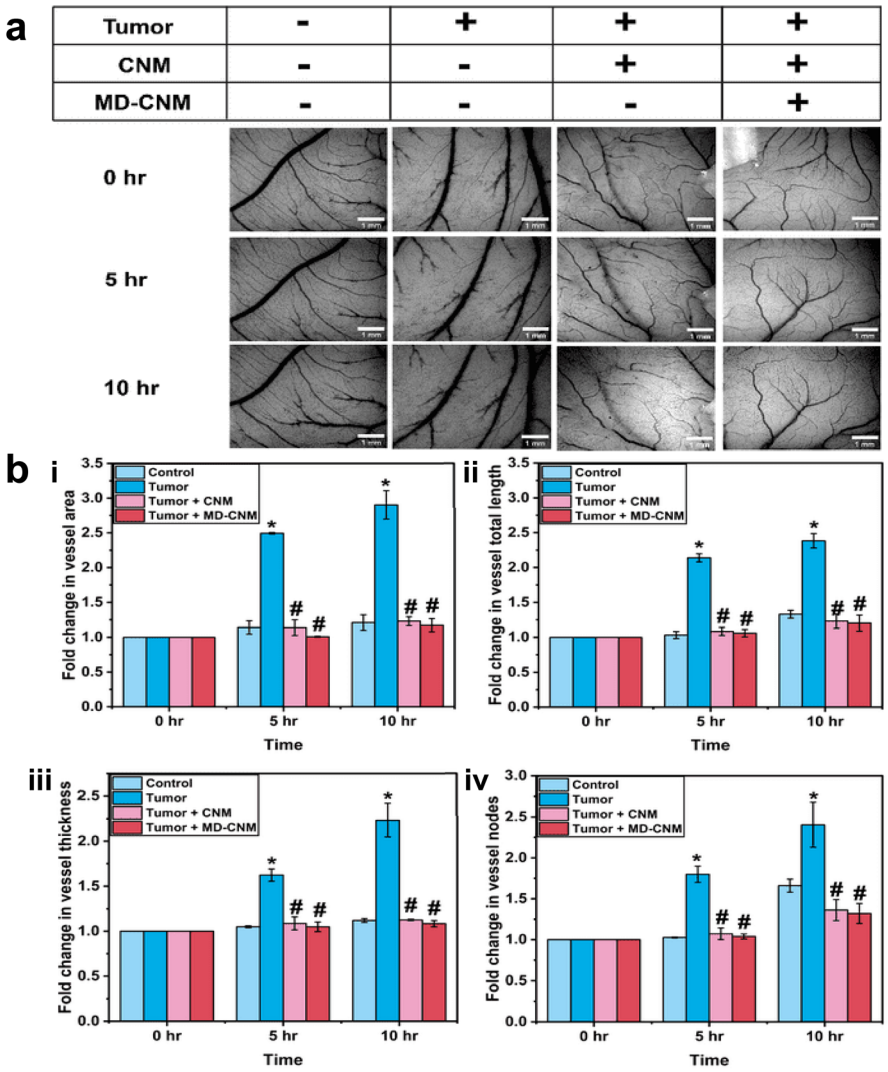

Fig. 10 (a) Post-processed images of CAM development chick embryo models at 0, 5, and 10 h with control, tumor alone, tumor + CNM, and tumor + MD-CNM. (b) Graphs showing the blood vessel formation, as represented by angiogenic parameters such as fold change in the total area (i), total length (ii), thickness (iii), and branching point (iv). "*" indicates a significant increase compared to the control and "#" indicates a significant decrease compared to the tumor group. Differences are considered statistically significant at $p < 0.05$. Scale bar: 1 mm.

effects of the drug-loaded MOF. The data underscore the critical role of the embedded drugs cisplatin, doxorubicin, and 5-fluorouracil in inhibiting angiogenesis.

Cisplatin is known to induce oxidative stress in endothelial cells, impairing their proliferation and migration, thereby reducing vessel formation.[83] 5-Fluorouracil modulates the tumor microenvironment by inhibiting matrix metalloproteinases (MMPs), essential for extracellular matrix remodeling and angiogenesis.[84] Doxorubicin suppresses vascular endothelial growth factor (VEGF) expression, disrupting endothelial cell signaling and reducing vessel growth.[85] The combination of these drugs likely creates a synergistic effect, amplifying the inhibition of angiogenesis. Additionally, the cytotoxic effects of cobalt and nickel ions are often linked to their ability to regulate gene expression related to apoptosis. For instance, studies have reported downregulation of anti-apoptotic genes (like Bcl-2) and upregulation of pro-apoptotic genes (like Bax and caspases) in response to treatment with cobalt-containing nanocarriers, enhancing the apoptosis rate in MDA-MB-231 cells.[86] The sustained drug release from MD-CNM ensures continuous therapeutic action over time. This extended inhibition of angiogenesis is crucial in reducing the tumor's blood supply, limiting growth and metastasis. Significant reduction in vessel nodes and branching points further reflects the suppression of capillary sprouting, highlighting the efficacy of MD-CNM as an anti-angiogenic agent. As a result, the MD-CNM significantly reduced angiogenesis compared to the tumor and CNM groups, as evidenced by reductions in the vessel area, length, thickness, and nodes. These findings demonstrate the potential of multidrug-loaded CNM as an effective strategy for inhibiting tumor angiogenesis and underscore its promise in anti-cancer therapy.

3.6.1. Anti-angiogenetic effect of MD-CNM downregulating VEGFA, FGF2, and ANG1 expression. To further investigate the

effect of MD-CNM at the genetic level, the mRNA expression of key angiogenesis-related genes was analyzed using RT-PCR in the CAM model. Angiogenesis, forming new blood vessels from the existing vasculature, is critical in tumor growth and metastasis. The process is tightly regulated by a balance of pro-angiogenic and anti-angiogenic factors.[82] Among the most critical pro-angiogenic regulators are VEGFA, FGF2, and ANG1, which synergistically promote endothelial cell proliferation, migration, and stabilization of newly formed vessels. As shown in Fig. 11, in tumor-induced samples, a substantial upregulation of VEGFA, FGF2, and ANG1 was observed, with VEGFA expression increasing approximately by fivefold (Fig. 11). VEGFA not only stimulates endothelial cell migration but also enhances the expression of other pro-angiogenic factors, creating a feed-forward loop that drives angiogenesis within the tumor microenvironment (TME). In Fig. 11, FGF2, another potent angiogenic factor, was upregulated fourfold, suggesting its role in promoting the proliferation of endothelial cells and the formation of capillary-like structures. ANG1, which is vital for vessel stabilization and maturation, showed a 4.5-fold increase, indicating that tumors actively enhance vascular integrity to ensure a consistent supply of oxygen and nutrients, supporting their growth and metastasis (Fig. 11).

Treatment with MD-CNM demonstrated remarkable anti-angiogenic effect by significantly downregulating the expression of VEGFA, FGF2, and ANG1 genes, which correspondingly reduced by 2-, 1.8-, and 2-fold compared to the tumor group. This is similar and comparable to the positive control, Avastin (tumor + Avastin), where the downregulation of VEGFA, FGF2, and ANG1 genes was 2.24-, 1.58-, and 3.75-fold, respectively, as compared to the tumor group. VEGFA downregulation disrupts the endothelial migration necessary for the formation of new capillaries, directly impairing the initial stages of angiogenesis. The suppression of FGF2 expression further inhibits endothelial cell proliferation, limiting the expansion of vascular networks within the TME.[87] ANG1 downregulation is particularly noteworthy as it destabilizes the already-formed vasculature, leading to a breakdown of vessel integrity and disrupting the tumor's ability to establish a stable blood supply. Additionally, CNM alone also exhibited cytotoxicity against MDA-MB-231 breast cancer cells, highlighting its inherent anti-cancer properties. Research indicates that cobalt–nickel MOFs can exhibit enhanced cytotoxicity compared to other formulations. For instance, specific cobalt–nickel formulations are more effective against MDA-MB-231 cells than traditional chemotherapeutic agents, highlighting their potential as alternative therapeutic options.[86] The ability of MD-CNM to inhibit VEGFA expression suggests its potential to interfere with hypoxia-driven signaling pathways commonly activated in tumors. Furthermore, the simultaneous downregulation of FGF2 and ANG1 highlights the multi-targeted action of MD-CNM, addressing both the initiation and stabilization phases of angiogenesis.[88] In addition to MD-CNM treatment, a positive control group receiving Avastin (tumor + Avastin) was included to benchmark the anti-angiogenic activity. RT-PCR analysis (Fig. 11) showed significant downregulation of angiogenic markers (VEGFA, FGF2, and ANG1) in this group, supporting the reliability of the CAM model and validating MD-CNM's comparable anti-angiogenic potential.[49]

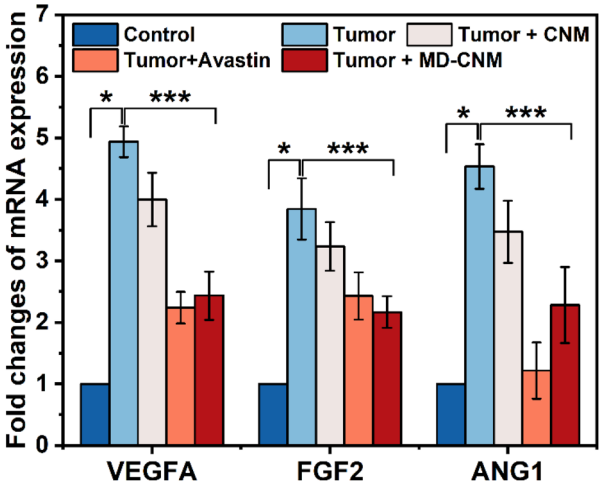

Fig. 11 Bar graphs showing the fold changes in gene expression of selected markers VEGFA, FGF2, and ANG1. The symbol "*" indicates a significant increase compared to the control and "***" indicates a significant decrease compared to the tumor.

This dual-action mechanism not only inhibits the formation of new vasculature but also disrupts the structural integrity of the existing tumor blood vessels. The resulting reduction in blood vessel density and stability can effectively starve the tumor of essential nutrients and oxygen, impeding its growth and metastatic potential.

The ability of MD-CNM to modulate the key angiogenic factors underscores its therapeutic potential in addressing the challenges of tumor angiogenesis. By targeting multiple pathways involved in vascular formation and stabilization, the MD-CNM presents a novel strategy for anti-cancer therapy. This approach not only suppresses angiogenesis but also reduces the likelihood of the resistance mechanisms often observed with single-target therapies. The findings provide a strong foundation for further exploration of MD-CNM as a multidrug platform with robust anti-angiogenic and anti-tumor effects. Recent reports highlight the role of m6A modifications in TNBC progression, wherein a study has reported that METTL3-mediated m6A methylation stabilizes KIF15 mRNA, promoting TNBC aggressiveness.[89] While our current study focused on classical angiogenic regulators (VEGFA, FGF2, and ANG1), these findings underscore the need to explore whether MOF-based systems like MD-CNM can be adapted to modulate epitranscriptomic targets for better clinical translation.

4 Conclusions

This study demonstrates the potential of cobalt–nickel metal–organic frameworks (CNMs) as a promising multidrug carrier for triple negative breast cancer (TNBC) therapy, addressing key challenges such as drug resistance in cancer treatment. The CNM demonstrated superior multidrug loading capacity, and the multidrug loaded CNM (MD-CNM) exhibited sustained drug

release for 96 h in PBS at physiological pH 7.4 and a faster release profile at acidic pH 6 that mimics the tumour microenvironment. Furthermore, the MOFs showed biocompatibility in normal cells and effectively induced necro-apoptosis in multidrug-resistant breast cancer cells at lower concentrations as compared to the individual drug-loaded MOF. Furthermore, *ex ovo* studies confirmed that the MD-CNM suppressed tumor-induced angiogenesis and downregulated the key pro-angiogenic genes (VEGFA, FGF2, and ANG1), demonstrating potential to inhibit tumor growth and metastasis. Collectively, these findings underscore the potential of CNMs as an innovative and efficient multidrug delivery platform, presenting a therapeutic strategy for combating multidrug-resistant cancer.

Data availability

Data will be made available on request.

Author contributions

Shaik Sameer Basha: writing – review & editing, writing – original draft, visualization, validation, resources, methodology, investigation, formal analysis, data curation. Abhishek Sasmal: writing – review & editing, writing – original draft, visualization, validation, resources, methodology, investigation, formal analysis, data curation. Subastri Ariraman: writing – review & editing, writing – original draft, validation, methodology. Mukilarasi B: methodology, writing – review. Thilak Raj: writing – review & editing. Vimalraj Selavaraj: validation, methodology, writing. A. Arockiarajan: writing – review & editing, supervision, resources, methodology, investigation, funding acquisition, formal analysis, conceptualization. Swathi Sudhakar: writing – review & editing, visualization, validation, supervision, resources, project administration, methodology, investigation, funding acquisition, formal analysis, conceptualization.

Conflicts of interest

The authors declare that there is no conflict of interest.

Acknowledgements

We are grateful for the financial support from IIT Madras through the Institutions of Eminence (IoE) Scheme (SP2223124CPETWOCSMHOC) from the Ministry of Education, Government of India, SP23242582AMSERB009000, SERB, Department of Science and Technology, India. The authors also thank Prof. Pijush Gosh for providing the FTIR facility and Prof. Saumendra Kumar Bajpai for the fluorescence microscope facility. The authors thank the Cancer Institute (WIA) Adyar, Chennai, for the FACS facility. Abhishek Sasmal acknowledges the Institute Post-Doctoral Fellowship scheme of IIT Madras for providing financial support. A. Arockiarajan gratefully acknowledges the Institute of Eminence Research Initiative Project on Materials and Manufacturing for Futuristic Mobility (Project no. SB22231272MMMOEX008702) (IIT Madras).

References

1 E. C. Dietze, C. Sistrunk, G. Miranda-Carboni, R. O'Regan and V. L. Seewaldt, *Nat. Rev. Cancer*, 2015, **15**(4), 248–254.
2 S. Siddharth and D. Sharma, *Cancers*, 2018, **10**, 514.
3 L. Yin, J. J. Duan, X. W. Bian and S. C. Yu, *Breast Cancer Res.*, 2020, **22**, 1–13.
4 W. D. Foulkes, I. E. Smith and J. S. Reis-Filho, *N. Engl. J. Med.*, 2010, **363**, 1938–1948.
5 P. Zagami and L. A. Carey, *npj Breast Cancer*, 2022, (8), 1–10.
6 X. Ma, H. Cheng, J. Hou, Z. Jia, G. Wu, X. Lü, H. Li, X. Zheng and C. Chen, *Chin. Opt. Lett.*, 2020, **18**, 051701.
7 J. Pang, N. Ding, X. Liu, X. He, W. Zhou, H. Xie, J. Feng, Y. Li, Y. He, S. Wang and Z. Xiao, *Ann Surg Oncol.*, 2024, **32**, 750–759.
8 P. Ferrari, C. Scatena, M. Ghilli, I. Bargagna, G. Lorenzini and A. Nicolini, *Int. J. Mol. Sci.*, 2022, **23**, 1665.
9 J. M. Lebert, R. Lester, E. Powell, M. Seal and J. McCarthy, *Curr. Oncol.*, 2018, **25**, 142–150.
10 N. Vasan, J. Baselga and D. M. Hyman, *Nature*, 2019, (575), 299–309.
11 D. Galmarini, C. M. Galmarini and F. C. Galmarini, *Crit Rev Oncol Hematol.*, 2012, **84**, 181–199.
12 S. Li, C. Bao, L. Huang and J. F. Wei, *J. Clin. Med.*, 2022, **11**, 6021.
13 L. A. Huppert, O. Gumusay and H. S. Rugo, *Ther. Adv. Med. Oncol.*, 2022, **14**, DOI: 10.1177/17588359221086916.
14 Z. Ai, B. Liu, J. Chen, X. Zeng, K. Wang, C. Tao, J. Chen, L. Yang, Q. Ding and M. Zhou, *Int. J. Pharm.*, 2024, 100314.
15 K. V. Babunagappan, A. Seetharaman, S. Ariraman, P. B. Santhosh, J. Genova, N. P. Ulrih and S. Sudhakar, *Nanoscale Adv.*, 2024, **6**, 2026–2037.
16 S. Lakkadwala, B. dos Santos Rodrigues, C. Sun and J. Singh, *J. Controlled Release*, 2019, **307**, 247–260.
17 X. Wei, L. Liu, X. Li, Y. Wang, X. Guo, J. Zhao and S. Zhou, *J. Controlled Release*, 2019, **313**, 42–53.
18 F. Greco and M. J. Vicent, *Adv. Drug Delivery Rev.*, 2009, **61**, 1203–1213.
19 A. Jędrzak, B. F. Grześkowiak, E. Coy, J. Wojnarowicz, K. Szutkowski, S. Jurga, T. Jesionowski and R. Mrówczyński, *Colloids Surf., B*, 2019, **173**, 698–708.
20 M. Liong, J. Lu, M. Kovochich, T. Xia, S. G. Ruehm, A. E. Nel, F. Tamanoi and J. I. Zink, *ACS Nano*, 2008, **2**, 889–896.
21 T. Baby, Y. Liu, A. P. J. Middelberg and C. X. Zhao, *Chem. Eng. Sci.*, 2017, **169**, 128–139.
22 S. Hua, M. B. C. de Matos, J. M. Metselaar and G. Storm, *Front. Pharmacol.*, 2018, **9**, 403086.
23 J. W. Shreffler, J. E. Pullan, K. M. Dailey, S. Mallik and A. E. Brooks, *Int. J. Mol. Sci.*, 2019, **20**, 6056.
24 M. Elsabahy and K. L. Wooley, *Chem. Soc. Rev.*, 2012, **41**, 2545–2561.
25 P. Mena-Giraldo, S. Pérez-Buitrago, M. Londoño-Berrío, I. C. Ortiz-Trujillo, L. M. Hoyos-Palacio and J. Orozco, *Sci. Rep.*, 2020, (10), 1–12.
26 P. M. Perrigue, R. A. Murray, A. Mielcarek, A. Henschke and S. E. Moya, *Pharmaceutics*, 2021, **30**(6), 770.

27 H. Yuan, Y. Chen, Y. Hu, Y. Li, H. Zhang, S. Zhang, Q. Chen, W. Zhou, J. Sun, Z. He, Y. Wang and C. Luo, *J. Pharm. Invest.*, 2025, 1–14.
28 Z. Wang, X. Wang, W. Xu, Y. Li, R. Lai, X. Qiu, X. Chen, Z. Chen, B. Mi, M. Wu and J. Wang, *Pharmaceutics*, 2023, **15**, 2623.
29 D. Zou, L. Yu, Q. Sun, Y. Hui, J. Teng, Y. Liu, G. Yang, D. Wibowo and C. X. Zhao, *Colloids Surf., B*, 2020, **193**, 111108.
30 N. S. Portillo-Vélez, J. L. Obeso, J. A. de los Reyes, R. A. Peralta, I. A. Ibarra and M. T. Huxley, *Commun. Mater.*, 2024, (5), 1–15.
31 V. F. Yusuf, N. I. Malek and S. K. Kailasa, *ACS Omega*, 2022, **7**, 44507–44531.
32 D. Ma, G. Wang, J. Lu, X. Zeng, Y. Cheng, Z. Zhang, N. Lin and Q. Chen, *Eur. J. Med. Chem.*, 2023, **261**, 115884.
33 Y. Feng, W. Wu and M. Li, *Front. Pharmacol.*, 2022, **13**, 1025780.
34 F. Xing, J. Xu, Y. Zhou, P. Yu, M. Zhe, Z. Xiang, X. Duan and U. Ritz, *Nanoscale*, 2024, **16**, 4434–4483.
35 M. U. Akbar, A. Akbar, U. A. K. Saddozai, M. I. U. Khan, M. Zaheer and M. Badar, *Mater. Adv.*, 2023, **4**, 5653–5667.
36 M. Ding, X. Cai and H. L. Jiang, *Chem. Sci.*, 2019, **10**, 10209–10230.
37 B. A. Akash, S. Kanagaraj, S. Sundaravadivelu, G. S. Varalakshmi, V. Manikantan, A. S. Pillai, A. Alexander and I. V. M. V. Enoch, *J. Mol. Struct.*, 2023, **1290**, 135906.
38 J. Senthilnathan, A. Arockiarajan, M. Yoshimura, J. B. Wagner, A. Sasmal, J. Senthilnathan, A. Arockiarajan and M. Yoshimura, *Nanomaterials*, 2023, **13**, 1098.
39 M. P. Kai, A. W. Keeler, J. L. Perry, K. G. Reuter, J. C. Luft, S. K. O'Neal, W. C. Zamboni and J. M. Desimone, *J. Controlled Release*, 2015, **204**, 70–77.
40 A. T. Lucas, S. K. O'Neal, C. M. Santos, T. F. White and W. C. Zamboni, *J. Pharm. Biomed. Anal.*, 2016, **119**, 122–129.
41 I. A. Alsarra and M. N. Alarifi, *J. Chromatogr. B*, 2004, **804**, 435–439.
42 S. S. Basha, K. V. Babunagappan, A. Kabir, T. Raj and S. Sudhakar, *J. Drug Delivery Sci. Technol.*, 2024, **98**, 105869.
43 K. V. Babunagappan, T. Raj, A. Seetharaman, S. Ariraman and S. Sudhakar, *J. Mater. Chem. B*, 2024, **12**, 4843–4853.
44 P. Kumar, A. Nagarajan and P. D. Uchil, *Cold Spring Harb. Protoc.*, 2018, **2018**, prot095505.
45 S. Ariraman, A. Seetharaman, K. V. Babunagappan and S. Sudhakar, *Mater. Adv.*, 2024, **5**, 6944–6956.
46 P. Nowak-Sliwinska, T. Segura and M. L. Iruela-Arispe, *Angiogenesis*, 2014, **17**, 779–804.
47 S. S. Basha, A. Sasmal, V. Selvaraj, S. Ariraman, B. Mukilarasi, C. K. Sahoo, A. Arockiarajan and S. Sudhakar, *ACS Appl. Polym. Mater.*, 2025, **7**, 4204–4217.
48 A. Kumar, S. S. Basha, M. B, V. Selvaraj, P. Ghosh and S. Sudhakar, *Int. J. Biol. Macromol.*, 2025, **267**, 144701.
49 S. Vimalraj, S. Bhuvaneswari, S. Lakshmikirupa, G. Jyothsna and S. Chatterjee, *Microvasc. Res.*, 2018, **119**, 47–59.
50 S. Vimalraj, N. C. Partridge and N. Selvamurugan, *J. Cell. Physiol.*, 2014, **229**, 1236–1244.
51 L. Jiao, J. Y. R. Seow, W. S. Skinner, Z. U. Wang and H. L. Jiang, *Mater. Today*, 2019, **27**, 43–68.
52 P. Horcajada, C. Serre, M. Vallet-Regí, M. Sebban, F. Taulelle and G. Férey, *Angew Chem. Int. Ed. Engl.*, 2006, **45**, 5974–5978.
53 D. M. Chen, N. N. Zhang, C. Sen Liu, Z. H. Jiang, X. D. Wang and M. Du, *Inorg. Chem.*, 2017, **56**, 2379–2382.
54 Y. Wang, J. Yan, N. Wen, H. Xiong, S. Cai, Q. He, Y. Hu, D. Peng, Z. Liu and Y. Liu, *Biomaterials*, 2020, **230**, 119619.
55 S. He, L. Wu, X. Li, H. Sun, T. Xiong, J. Liu, C. Huang, H. Xu, H. Sun, W. Chen, R. Gref and J. Zhang, *Acta Pharm. Sin. B*, 2021, **11**, 2362–2395.
56 J. Pandit, S. Singh and M. Muthu, *Ann. Indian Acad. Neurol.*, 2006, **9**, 207–216.
57 P. Fouladian, J. Kohlhagen, M. Arafat, F. Afinjuomo, N. Workman, A. Y. Abuhelwa, Y. Song, S. Garg and A. Blencowe, *Biomater. Sci.*, 2020, **8**, 6625–6636.
58 M. Yusefi, K. Shameli, H. Jahangirian, S. Y. Teow, H. Umakoshi, B. Saleh, R. Rafiee-Moghaddam and T. J. Webster, *Int. J. Nanomed.*, 2020, **15**, 5417–5432.
59 Y. Chen, W. Lu, M. Schröder and S. Yang, *Acc. Chem. Res.*, 2023, **56**, 2569–2581.
60 J. Zhu, L. Samperisi, M. Kalaj, J. A. Chiong, J. B. Bailey, Z. Zhang, C. J. Yu, R. E. Sikma, X. Zou, S. M. Cohen, Z. Huang and F. A. Tezcan, *Dalton Trans.*, 2022, **51**, 1927–1935.
61 I. Han, S. A. Choi, D. N. Lee, T. Thambi, C. Alonso-Moreno, I. Han, S. A. Choi and D. N. Lee, *Pharmaceutics*, 2022, **14**, 378.
62 J. Zhang, M. Li, M. Liu, Q. Yu, D. Ge, J. Zhang, J. Zhang, M. Li, M. Liu, Q. Yu, D. Ge and J. Zhang, *Nanomaterials*, 2024, **14**, 797.
63 S. Kundu, A. K. Swaroop and J. Selvaraj, *Curr. Top. Med. Chem.*, 2023, **23**, 1155–1170.
64 P. L. Falcão, B. M. Motta, F. C. de Lima, C. V. Lima and T. P. R. Campos, *Radiol. Bras.*, 2015, **48**, 158–165.
65 S. Parihari, A. Pant, A. Halder and S. Srivastava, *J Am Soc Mass Spectrom*, 2025, **36**(6), 1227–1240.
66 A. Paramanantham, E. J. Jung, H. J. Kim, B. K. Jeong, J. M. Jung, G. S. Kim, H. S. Chan and W. S. Lee, *Int. J. Mol. Sci.*, 2021, **22**, 12438.
67 Establishment of a 5-fluorouracil-resistant triple-negative breast cancer cell line, **https://www.spandidos-publications.com/10.3892/ijo.2013.2135**, (accessed 20 June 2025).
68 A. V. Snezhkina, A. V. Kudryavtseva, O. L. Kardymon, M. V. Savvateeva, N. V. Melnikova, G. S. Krasnov and A. A. Dmitriev, *Oxid. Med. Cell. Longev.*, 2019, 6175804.
69 Y. Yao, Y. Zhou, L. Liu, Y. Xu, Q. Chen, Y. Wang, S. Wu, Y. Deng, J. Zhang and A. Shao, *Front. Mol. Biosci.*, 2020, **7**, 558493.
70 S. Mirzaei, K. Hushmandi, A. Zabolian, H. Saleki, S. M. R. Torabi, A. Ranjbar, S. Seyedsaleh, S. O. Sharifzadeh, H. Khan, M. Ashrafizadeh, A. Zarrabi and K. S. Ahn, *Molecules*, 2021, **26**, 2382.
71 K. S. Chun and S. H. Joo, *Biomol. Ther.*, 2022, **30**, 479–489.

72 J. Heureaux-Torres, K. E. Luker, H. Haley, M. Pirone, L. M. Lee, Y. Herrera, G. D. Luker and A. P. Liu, *APL Bioeng.*, 2018, **2**, 032001.
73 P. Karna, P. C. G. Rida, V. Pannu, K. K. Gupta, W. B. Dalton, H. Joshi, V. W. Yang, J. Zhou and R. Aneja, *Cell Death Differ.*, 2010, **18**, 632–644.
74 D. S. Chulpanova, K. V. Kitaeva, L. G. Tazetdinova, V. James, A. A. Rizvanov and V. V. Solovyeva, *Front. Pharmacol.*, 2018, **9**, 344295.
75 F. Doonan and T. G. Cotter, *Methods*, 2008, **44**, 200–204.
76 Y. Gong, Z. Fan, G. Luo, C. Yang, Q. Huang, K. Fan, H. Cheng, K. Jin, Q. Ni, X. Yu and C. Liu, *Mol. Cancer*, 2019, **18**(1), 1–17.
77 M.-B. Meng, H.-H. Wang, Y.-L. Cui, Z.-Q. Wu, Y.-Y. Shi, N. G. Zaorsky, L. Deng, Z.-Y. Yuan, Y. Lu, P. Wang, M.-B. Meng, H.-H. Wang, Y.-L. Cui, Z.-Q. Wu, Y.-Y. Shi, N. G. Zaorsky, L. Deng, Z.-Y. Yuan, Y. Lu and P. Wang, *Oncotarget*, 2016, **7**, 57391–57413.
78 Z. Su, Z. Yang, L. Xie, J. P. Dewitt and Y. Chen, *Cell Death Differ.*, 2016, **23**(5), 748–756.
79 K. Vermeulen, D. R. Van Bockstaele and Z. N. Berneman, *Cell. Prolif.*, 2003, **36**, 131–149.
80 X. Chen, K. H. Low, A. Alexander, Y. Jiang, C. Karakas, K. R. Hess, J. P. W. Carey, T. N. Bui, S. Vijayaraghavan, K. W. Evans, M. Yi, D. C. Ellis, K. L. Cheung, I. O. Ellis, S. Fu, F. Meric-Bernstam, K. K. Hunt and K. Keyomarsi, *Clin. Cancer Res.*, 2018, **24**, 6594–6610.
81 I. A. Shaltiel, L. Krenning, W. Bruinsma and R. H. Medema, *J. Cell Sci.*, 2015, **128**, 607–620.
82 S. Vimalraj, T. Ashokkumar and S. Saravanan, *Biomed. Pharmacother.*, 2018, **105**, 440–448.
83 Y. T. Cheng, C. C. Yang and L. F. Shyur, *Pharmacol. Res.*, 2016, **114**, 128–143.
84 R. Ragoowansi, U. Khan, R. A. Brown and D. A. McGrouther, *Br. J. Plast. Surg.*, 2001, **54**, 283–287.
85 U. J. Yun, J. H. Lee, J. Shim, K. Yoon, S. H. Goh, E. H. Yi, S. K. Ye, J. S. Lee, H. Lee, J. Park, I. H. Lee and Y. N. Kim, *Lab. Invest.*, 2019, **99**(8), 1157–1172.
86 E. Jamshidifar, F. Eshrati Yeganeh, M. Shayan, M. Tavakkoli Yaraki, M. Bourbour, A. Moammeri, I. Akbarzadeh, H. Noorbazargan and N. Hossein-Khannazer, *Int. J. Mol. Sci.*, 2021, **22**, 7948.
87 S. Vimalraj, T. Ashokkumar and S. Saravanan, *Biomed. Pharmacother.*, 2018, **105**, 440–448.
88 T. Kamba and D. M. McDonald, *Br. J. Cancer*, 2007, **96**(12), 1788–1795.
89 C. Chen, Y. Wang, Y. Li and C. Zhang, *Discov. Med.*, 2023, **35**, 787–795.